
Performance Characteristics of a Whole-Body Positron Tomograph

Terence J. Spinks, Riccardo Guzzardi, and C. Riccardo Bellina

*MRC Cyclotron Unit, Hammersmith Hospital, London, UK and
CNR Institute of Clinical Physiology, Pisa, Italy*

This paper describes an investigation of some of the important physical characteristics of a whole-body positron tomograph consisting of two rings of bismuth germanate detectors of dimensions 5.6 mm × 30 mm × 30 mm (512/ring). The resolution applicable to in vivo imaging is six mm or more, depending on radionuclide and reconstruction filter and is very uniform over the field of view normally used. Axial resolution can be varied by moving side collimation (maximum ~16 mm FWHM with interplane septa). A simple scheme has been devised to correct for loss of true coincidence events with varying count rate based on the total random and multiple coincidence rates. It is concluded that correction for scattered radiation should be implemented for reliable quantitation.

J Nucl Med 29:1833-1841, 1988

The basic design considerations of the whole-body positron tomograph used in this study have been presented by Hoffman et al. (1). These emphasized features facilitating cardiac studies such as the ability to tilt and rotate the gantry, to align it with the axis of the heart, and also inputs for cardiac gating. A preliminary report on the use of the tomograph, particularly in cardiology, has been given by the same group (2). This demonstrated the clarity of anatomical features attainable in the heart as well as in the brain. Details of the various components of the data collection system have also been described in a number of articles (3-5).

For any tomographic study the correct interpretation of clinical data is dependent on an accurate knowledge of the physical limitations of the scanner. This paper presents the basic physical performance parameters of this device which affect the derivation of quantitative clinical data. It includes an investigation of transaxial and axial resolution, efficiency, linearity, and deadtime losses and presents a preliminary assessment of count recovery with object size and the influence of scattered radiation.

MATERIALS AND METHODS

Physical Construction of Tomograph

The tomograph consists of two rings each consisting of 512 closely-packed BGO detectors (ECAT III, Model 911, CTI

Inc., Knoxville, TN). The detector thickness (tangentially) is 5.6 mm with a center-to-center spacing of 6.1 mm. The crystal height (axially) and depth (radially) are both 30 mm. Each detector is viewed independently by a single 10-mm photomultiplier tube (Hamamatsu R-1635). There is 0.25 mm of aluminum between detectors in the same ring and six mm of steel between detectors in separate rings. The ring diameter is 100 cm (between opposing detector faces) and the distance between detector centers in the two rings is 36 mm. The interplane septum (manually removable in a number of sections which fit together to form an annulus) has a radial length of 17 cm and a thickness tapering from 12 mm at the detector end to 3 mm. The detector aperture can be varied by moving side collimation under computer control to give maximum and minimum apertures of 65 mm and 32 mm. These correspond to detector apertures of 29.5 and 13 mm, respectively, (septum out) and 26.5 and 10 mm (septum in). Lead shielding is provided at the sides of the detectors.

The opening for the patient is 65 cm in diameter which is sufficient to accommodate rotation and tilting of up to 30°. The required position on the patient's body is set using a crossed laser beam—the laser source being mounted on the gantry. All gantry and bed (horizontal and vertical) motions are monitored by the host computer (DEC-Vax 11/730). Three image planes can be obtained simultaneously, two using coincidence events recorded within each ring (direct planes) and one using events between one ring and the other (cross plane).

Data Collection and Processing

The detectors in each ring are grouped into 16 buckets (32 detectors per bucket). In this study, each bucket was operated in coincidence with seven buckets on the opposite side of the ring, and data acquisition was carried out with the detectors stationary (as opposed to wobble mode). The latter was not

Received Aug. 14, 1987; revision accepted June 27, 1988.

For reprints contact: T.J. Spinks, PhD, MRC Cyclotron Unit, Hammersmith Hospital, Du Cane Rd., London W12 0HS, U.K.

used in clinical studies due to the large data storage requirements (four times that for stationary mode). The coincidence time window (2τ) is 24 nsec. All coincidences recorded between opposing "buckets" within the 24 nsec window are termed "prompt" coincidences (P). They are a combination of true coincidences (T), which arise from the same positron emission, and random coincidences (R) from unrelated gamma rays. Randoms are continuously monitored by forming coincidences in a 24 nsec time window with a delay of 48 nsec between opposing detectors. The random rate is subtracted from the prompt rate automatically to give the true rate. The third category of event is the multiple (M) which results from three or more events occurring within the 24 nsec window. The energy threshold used in the present study was 250 keV. The measured total coincidence count rate TOT (as reported during data acquisition) is given by:

$$\text{TOT} = \text{P} + \text{R} + \text{M} = \text{T} + 2\text{R} + \text{M} \quad (1)$$

True coincidence events are sorted into sinograms in a real-time sorter (RTS) (3). Use of the RTS necessitates the definition of the number of frames (limited by the RTS memory) and the time per frame before the commencement of scanning. As soon as the scanning period is over, the sinograms are transferred to magnetic disk. Reconstruction can be performed with an operator-selectable choice of filter functions (ramp, Butterworth, Hann, Hamming, and Parzen) and cutoff frequencies. The image matrix size is operator-selectable (into 256×256 , 128×128 , or 64×64 pixels) as is the mm/pixel.

Correction for photon attenuation can be carried out by calculation or measurement. In the standard software, calculated correction assumes an elliptical object of uniform attenuation, the dimensions and attenuation coefficient of which are selected by the operator. Measured attenuation correction is effected by the use of a ring source of activity which fits just inside the patient port. It is in the field of view (FOV) of the detectors but outside the reconstructed FOV. The source consists of a closely-packed helix of polythene tubing wound round a plastic ring which is inserted manually. The axial dimension is ~ 10 cm which well covers the detector aperture. For the tests described it was filled with gallium-68 (^{68}Ga) solution. The ^{68}Ga ($t_{1/2} = 68.3$ min) was obtained from a $^{68}\text{Ge}/^{68}\text{Ga}$ generator. Germanium-68 (^{68}Ge) decays by electron capture to produce the positron-emitter ^{68}Ga . Periodically, the detector efficiencies were normalized by inserting a plane source of ^{68}Ge ($t_{1/2} = 270$ days) into the FOV. The source is scanned at six angles (movement being automatically controlled). Relative efficiencies for each coincidence line-of-response are placed into a file for use in subsequent reconstructions.

Spatial Resolution

Transaxial (in-plane) resolution (full width at half and tenth maximum—FWHM and FWTM) was measured using Polythene tubing of internal and external diameters 1.0 and 1.5 mm, respectively, inserted (axially) into close-fitting holes in a Plexiglas cylinder of diameter 30 cm. This set-up was used to simulate the positron range in *in vivo* studies. Measurements were carried out with the line sources (containing either nitrogen-13 (^{13}N) or ^{68}Ga to investigate the effect of different positron energies) in the center of the tomographic FOV and at 6, 12, and 18 cm from the center. Data was acquired (as in

in vivo studies) in stationary mode with interplane septum inserted and with a collimator aperture of 65 mm. Measured correction for attenuation was applied and images were reconstructed both with ramp and Hann filters (cutoff frequency 0.5 of Nyquist) (6).

About 500k total true events per plane were acquired for each emission scan. At least 20 million true events per direct plane (40 million cross plane) were acquired for both blank (no object in FOV) and transmission scans using the external ^{68}Ga ring source. These figures were based on investigation of the variation in the standard deviation of pixel counts in emission images of a uniform phantom for different numbers of counts in transmission and blank scans. This applies to all measured attenuation corrections carried out in this study. Spatial resolution was calculated by taking a profile through the center of the image of the line source and using a linear interpolation.

Axial resolution was measured by placing a $^{68}\text{Ge}/^{68}\text{Ga}$ steel needle perpendicular to the axis of the scanner in air and performing a rectilinear scan as the patient bed was passed through the FOV in steps of 1 mm. At each position (0, 6, 12, and 18 cm from the center of the FOV) more than 200k true events were collected. Data was collected with the interplane septum both in place and removed.

Efficiency, Count Rate Performance, and Deadtime

The basic assessment of efficiency of the tomograph was carried out with a circular cylinder 20 cm in diameter and length which was filled uniformly with ^{68}Ga solution. Efficiency was defined as recorded true coincidence counts/sec/ $\mu\text{Ci/ml}$. The specific activity of an aliquot of the solution was measured in a calibrated ionization chamber. The cylinder was placed centrally in the FOV and data acquired for low specific activity ($\sim 0.1 \mu\text{Ci/ml}$) so that deadtime correction was negligible (see below and results section). Random, multiple, and total [TOT – Eq. (1)] count rates were also recorded over a range of specific activities up to about $0.7 \mu\text{Ci/ml}$. Data was obtained with septum in and out.

Deadtime losses were defined by the change in measured efficiency with changing specific activity for three source geometries. These were (a) a uniform cylinder, (b) a tube source in a scattering medium, and (c) a heart phantom. The uniform cylinder was of diameter 24 cm and length 12 cm. The second phantom consisted of a tube of diameter 1.6 cm and length 12 cm inserted into a rectangular Plexiglas block of dimensions 20 cm \times 20 cm \times 15 cm (7). The heart phantom comprised two concentric Plexiglas spheres (diameters 6 cm and 8 cm) supported by Plexiglas plates (in the axial direction) within a rectangular tank of dimensions 32 cm (length-axial) 26 cm (width) \times 15 cm (height). The tank was filled with sawdust to simulate the lungs. The inner sphere (cavity) was filled with active solution and the volume between the spheres (myocardium) was filled with water. The maximum activity in each phantom (either ^{68}Ga or ^{13}N) was chosen to give a total count rate close to or just above the maximum data transfer rate from coincidence processor to buffer memory ($\sim 600\text{k counts/sec}$).

True, random, and multiple count rates were again recorded for each of these tests. For the uniform cylinder, mean counts/pixel in the image were also obtained from a circular region of interest (ROI) of diameter 15 cm in the center of the phantom. Images were reconstructed with measured atten-

uation correction and the Hann filter. Measurements were carried out for each phantom with the septum inserted and with the maximum collimator aperture (65 mm).

Linearity

The relationship between counts/pixel and specific activity was examined with a "PIE" phantom consisting of a Plexiglas circular cylinder of diameter 24 cm and length 12 cm divided into six equal 60° sectors. Specific activities (^{68}Ga) in the sectors were approximately in the ratios 0:1:2:3:4:5. The precise ratios were determined by withdrawing five 0.5 ml samples from each sector after scanning and counting them in a well counter. Data was acquired at two count rates; the higher rate was 17k cps trues (direct plane) and 30k cps trues (cross plane) while the lower rate was 7k cps (direct) and 13k cps (cross). A circular ROI of diameter 45 mm (1.0 mm/pixel) was defined in each sector. Measured attenuation correction was applied.

Scatter

The influence of scattered radiation on a reconstructed image was carried out with the PIE and heart phantoms. Data were acquired with septum inserted. The PIE phantom was scanned (a) with one sector active and the remainder filled with water and (b) after the water had been emptied out. Counts/pixel (ROI diameter 37 mm, 1.5 mm/pixel) at different positions in the cold regions (five inactive sectors) were expressed as a percentage of that in the center of the hot region. The effect on quantitation was assessed by comparing counts/pixel in the active sector for the two situations (surrounded by water or not). For the heart phantom the central sphere (cavity) was filled with active solution and the outer myocardium with water (and vice versa), and it was scanned within the tank emptied or filled with water. Again counts/pixel were compared (ROI diameter 11 mm, 0.6 mm/pixel). The ratio between counts/pixel in a ROI in the center of the "cold" cavity and counts per pixel in the "hot" myocardium was calculated. This ratio was compared with and without surrounding water. In all cases, attenuation correction was measured and data were corrected for decay and deadtime in emission, transmission, and blank scans (as will be described below). Images were reconstructed with the Hann filter.

Recovery Coefficients

The variation in count recovery with object size was investigated with two geometrical configurations. The first was a simulation of the heart (different from that described above) comprising a Plexiglas cylinder of diameter 10.5 cm and length 12 cm with a second cylinder of diameter 7.0 cm placed inside it. The axes were parallel but separated by 1.6 cm. The volume between the two cylinders represented a myocardial wall with thickness varying from 2 mm to 33 mm. It was filled with ^{68}Ga solution and the inner cylinder (representing the ventricular chamber) with water. Forty circular ROIs of diameter 6 mm were drawn on a circle described around the center of the myocardial chamber. Ramp and Hann filters were used in reconstruction.

The second phantom consisted of a hollow Plexiglas wedge of internal height 19 cm (transaxial), length 12 cm (axial), and whose internal thickness varied from 0 to 25 mm. It was held within a cylinder whose axis was parallel to the length of the wedge and to the axis of the tomograph. The wedge was filled alternately with ^{13}N and ^{68}Ga and the surrounding volume

was either water-filled or empty. Profiles of width 1 and 3 pixels (1 mm/pixel) were drawn through the center of the triangular image of the wedge (parallel to its height).

Image Quality

An impression of the overall quality of the images produced by the tomograph was obtained with a multi-line-source phantom (8). This was a solid Plexiglas cylinder divided into six sectors each containing a set of holes drilled parallel to the axis; the holes were uniformly spaced in each sector with spacing proportional to hole size. The diameters ranged from 2.5 mm to 6.25 mm and the spacings (between hole centers) from 10 mm to 25 mm. The holes were filled with ^{13}N solution of the same specific activity and, as in vivo studies, data was acquired in stationary mode and attenuation correction measured. Ramp and Hann filters were used in reconstruction.

RESULTS

Spatial Resolution

Values of FWHM (mm) for a direct plane are shown in Table 1. Results for other planes differed by only ~ 0.1 mm. Mean FWHM values for ^{13}N , (radial, tangential, and different filters) is 0.5 ± 0.1 mm lower than for ^{68}Ga . This reflects the effect of difference in positron energy ($E_{\text{max}} = 1.2$ MeV for ^{13}N and 1.9 MeV for ^{68}Ga). The ramp filter gives, on average, an FWHM 2.4 ± 0.4 mm lower than the Hann filter (combining all ^{13}N and ^{68}Ga data).

The variation in axial resolution (FWHM) is shown in Table 2 both for a direct and cross plane with septum inserted and removed. With the septum inserted and side collimation fully opened, the axial FWHM (at the center of the FOV) is about twice the transaxial resolution (FWHM) using the Hann filter (Table 1).

Efficiency, Count Rate Performance, and Dead Time

The mean efficiency for the direct planes, measured with the 20 cm diameter uniform cylinder, septum removed, and a lower energy threshold of 250 keV, is 57k cps/ $\mu\text{Ci/ml}$ while that for the cross plane is 109k

TABLE 1
Measurements of Transaxial Resolution with Plastic Tube Sources (Stationary Sampling)

Distant from center of FOV (cm)	Transaxial resolution (FWHM) in mm							
	^{13}N				^{68}Ga			
	Hann		Ramp		Hann		Ramp	
	R*	T†	R	T	R	T	R	T
0	8.4	8.5	5.9	5.9	8.7	8.9	6.3	6.2
6	8.6	8.5	6.1	5.9	9.0	9.0	6.7	6.6
12	8.7	9.1	6.5	6.4	9.1	9.6	7.0	7.1
18	9.8	9.9	8.6	7.5	—	—	—	—

* Radial.

† Tangential.

TABLE 2
Measurements of Axial Resolution at Different Distances from the Center of the FOV

Distant from center of FOV (cm)	Axial resolution (FWHM) in mm			
	Direct plane		Cross plane	
	Septa in	Septa out	Septa in	Septa out
0	15.5	18.3	15.5	18.6
6	15.4	18.3	15.1	18.4
12	16.0	17.7	15.0	18.6
18	16.1	18.3	14.9	19.4

cps/ μ Ci/ml. This reflects the fact that cross plane data is derived from twice as many coincidence lines of response as for the direct plane but over a slightly different solid angle. Corresponding figures for septa inserted are 38k cps/ μ Ci/ml (direct) and 67k cps/ μ Ci/ml (cross). The differences between septa in and out are due partly to simple reduction of the detector aperture and also to the elimination of some scatter events.

The relationships between true, random, and multiple coincidence rates for the 20 cm diameter uniform cylinder (septum out), expressed as a percentage of the total recorded rate [TOT—Eq. (1)], against TOT are shown in Figure 1. The data are for a direct plane up to a total rate of 80k cps. The true and random rates are equal at ~ 15 cps, at which point the multiple rate is ~ 7 k cps (total rate 50k cps). When the septum is inserted, true and random rates are equal at ~ 22 k cps with a corresponding multiple rate of 8k cps (total rate 74k cps).

The multiple rate has been used previously as a parameter for estimating the loss of true coincidence events (9). Figure 2A shows the relationship between mean %DTL for all three planes (based on deviation between known and measured half-lives) and the total system multiple cps for the 24 cm diameter uniform cylinder (^{13}N), heart phantom (^{68}Ga), and tube source (^{13}N) within the Plexiglas block. The curves are similar for each geometry but there are small differences at a given multiple count rate for different geometries. Figure 2B, in contrast, is a plot of %DTL vs. the sum of total system multiple and random rates. It can be seen that the variation in DTL for a given multiple plus random rate is much less. The relationship can be seen to break down at a random plus multiple rate of ~ 300 k cps which corresponds to the maximum data transfer rate of the system.

Linearity

A plot of specific activity vs. counts/pixel for direct and cross planes is shown in Figure 3 for the PIE phantom at the two different counting rates. All data are corrected for decay to the same time. Good linearity is seen for both counting rates. The slightly greater scatter in the points at the lower rate is assumed to reflect the larger statistical error. In each case, there is a positive intercept on the y axis which is similar for the two count rates (i.e., positive counts/pixel in the inactive sector). This intercept, which is significantly different from zero ($p < 0.05$), is, on average, $5.3 \pm 1.1\%$ of the counts in the hottest sector. The difference

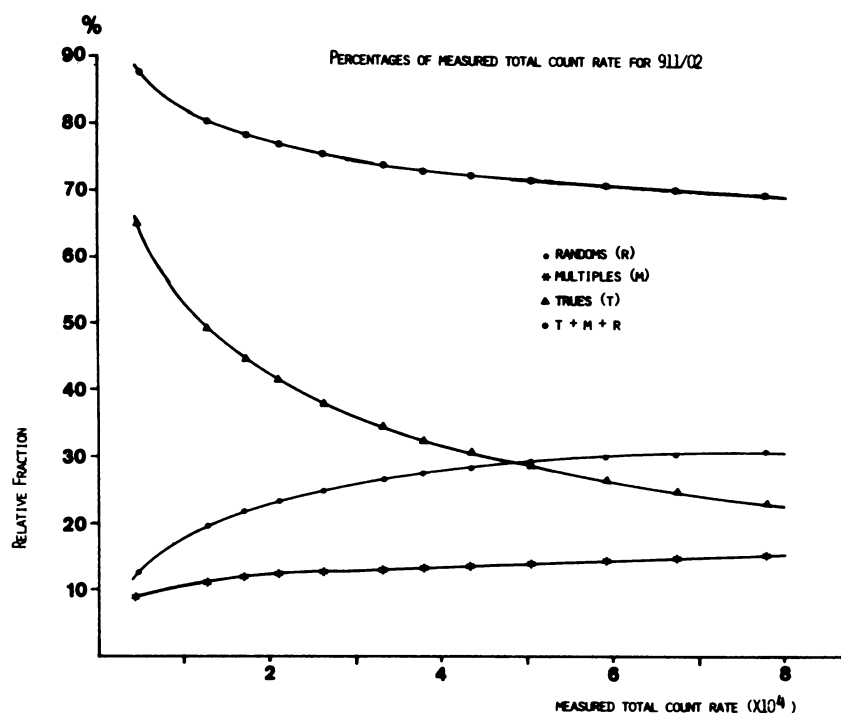


FIGURE 1
Variation of true, random and multiple coincidence count rates as a percentage of the total rate [TOT—Eq. (1)] for a uniform 20 cm diameter cylinder.

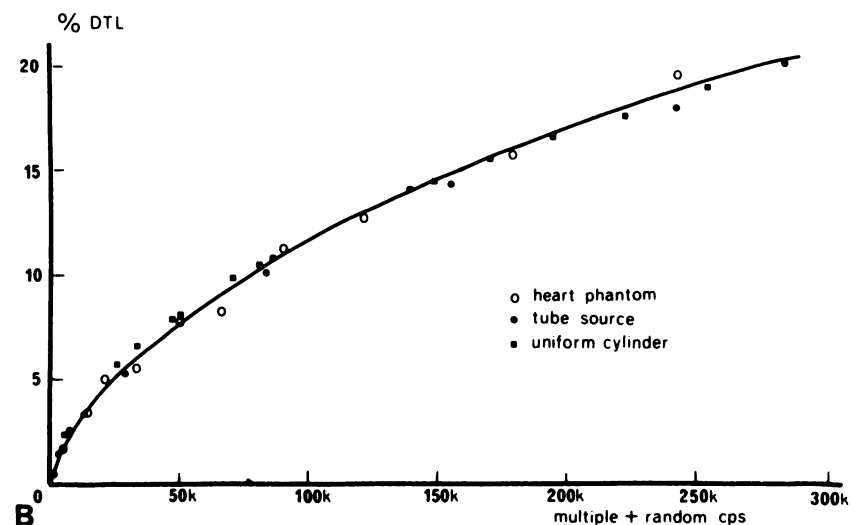
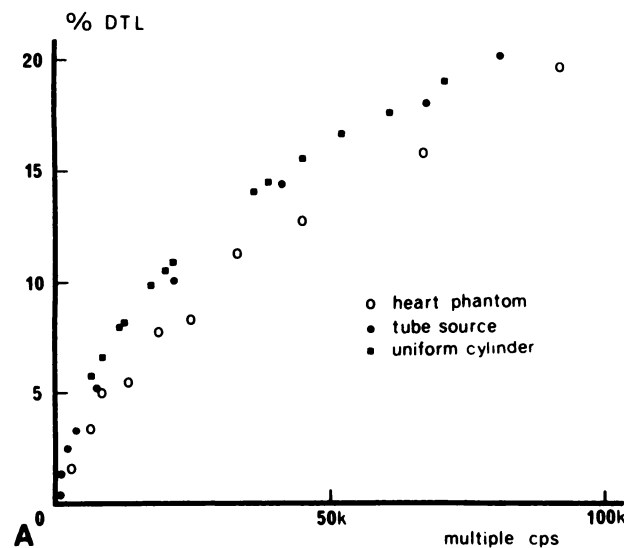


FIGURE 2
Relation between percentage dead time loss (%DTL) and (a) total system multiple cps and (b) the sum of total system random and multiple cps; DTL is obtained from the expression $DTL = 0.99 + 0.157x - 0.000642x^2 + 0.00000124x^3$ (where x = random plus multiple cps).

between calculated slopes for the two count rates is $<1\%$. The use of calculated attenuation correction makes no appreciable difference to the result.

Scatter

The data from the PIE phantom were used as a measure of the effect of scatter in reconstructed data. For the case of one active sector and the other sectors filled with water, maximum ROI counts/pixel in the cold region is $\sim 6\%$ of that in the hot region (near the hot region, but far enough away to eliminate spillover due to spatial resolution). This agrees well with the magnitude of the intercept for the linearity data above since the inactive and hottest sectors were, in that case, adjacent. Average counts/pixel over the five "cold" sectors is $2.1 \pm 1.5\%$ of the hot region. With the water sections emptied, the average counts/pixel is $0.5 \pm 1.3\%$.

The ratios between corrected cps/pixel (active region) for both PIE and heart phantoms with and without

water surrounding the active region are shown in Table 3. It was also, of course, possible to calculate the attenuation correction for the full PIE phantom but it can be seen that this makes no significant difference to the result. The ratio between "cold" cavity and "hot" myocardium pixel counts was 4.4% with water surrounding and 3.2% without.

Recovery Coefficients

A plot of counts/pixel against radial thickness of the "myocardium" for the cylindrical heart phantom (^{68}Ga) is shown in Figure 4A. The curves are normalized to the maximum value for the ramp filter. It appears that a plateau is reached beyond 25 mm where the two curves are very similar. Below 20 mm, there is a small but consistent difference between the two filters. Assuming full recovery beyond 25 mm, the recovery coefficients at 15 mm, 10 mm, and 5 mm are 98%, 89% and 51%, respectively, for the ramp and 94%, 82%, and 44% for the Hann filter.

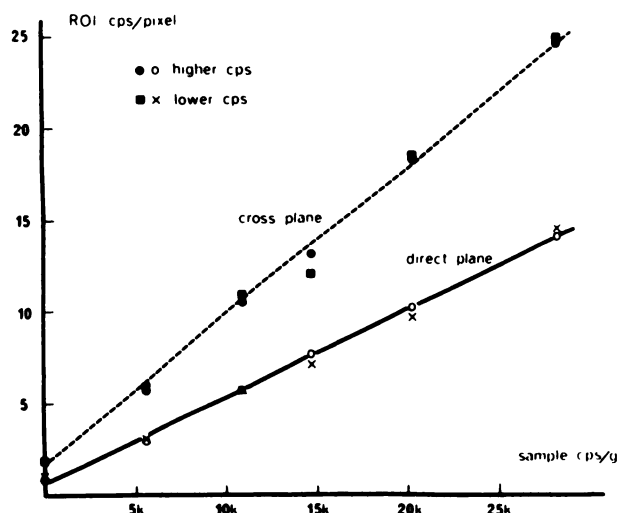


FIGURE 3
Relation between counts/pixel in various sectors of PIE phantom and relative specific activity for one direct plane and the cross plane. The higher and lower true coincidence cps per direct plane are 17k and 7k, respectively. Fitted lines are for the higher rate. The slopes for the lower rate only differ by 1%.

The influence of geometry on measured recovery is demonstrated in Figure 4B. This is a comparison of the curves obtained for the wedge (with and without water surrounding) and heart phantoms. The data are for ^{68}Ga and the Hann filter. Due to the restricted range of width in the wedge (maximum 25 mm), the plateau level is uncertain. Consequently each of the wedge curves has been normalized to the heart curve at 23 mm thickness (representing the peak values in the wedge curves). The wedge data was obtained from profiles 3 pixels (3 mm) wide; the data for 1 pixel width was insignificantly different. There are significant differences between the heart and wedge, and the presence or absence of water surrounding the wedge also affects the shape of the curves.

Figure 4C shows curves [normalized as in Fig. 4B)] for ^{13}N and ^{68}Ga in the wedge surrounded by water. Recovery coefficients for ^{13}N are ~5–7% higher than for ^{68}Ga over the range 5 to 15 mm.

Image Quality

Images of the multiple line source phantom reconstructed with the two filters are shown in Figures 5A and B. The smallest holes are resolved with the ramp but not with the Hann filter. These images give a good demonstration of decrease in count recovery with decreasing object size.

DISCUSSION

The constantly emphasized aim of positron tomography is to provide absolute quantitative measurements of physiological quantities in vivo. The realization of this goal is dependent, among other things, on an intimate knowledge of the physical characteristics and limitations of the tomograph.

Spatial resolution must be as uniform as possible over the object under study so that distortions do not occur. Count recovery with varying object size also depends directly on its magnitude. In addition, axial resolution (slice thickness) should match transaxial resolution as closely as possible so that improvement in one is not offset by degradation in the other. Second, one must have confidence that recorded image counts are linear with specific activity in a given object over the range of count rates encountered. A correction scheme to measure losses in recorded counts is essential. For a given activity distribution, it is also important that measured image counts per unit activity do not vary across the transaxial slice. This calls for the use of directly measured attenuation correction factors, particularly in cardiac and pulmonary studies. Third, a means

TABLE 3
Tests of the Effect of Scattering Medium on Quantitation

Phantom activity distribution	Surrounding scattering medium	Attenuation correction	Ratio of c/pix/sec/unit activity in active region—without/with water
PIE phantom one active sector	Water in five remaining sectors	Measured	1.13
		Calculated for full phantom	1.12
Heart phantom activity in central cavity	Water filling tank containing phantom	Measured	1.18
Heart phantom activity in "myocardial" cavity	Water filling tank containing phantom	Measured	1.16

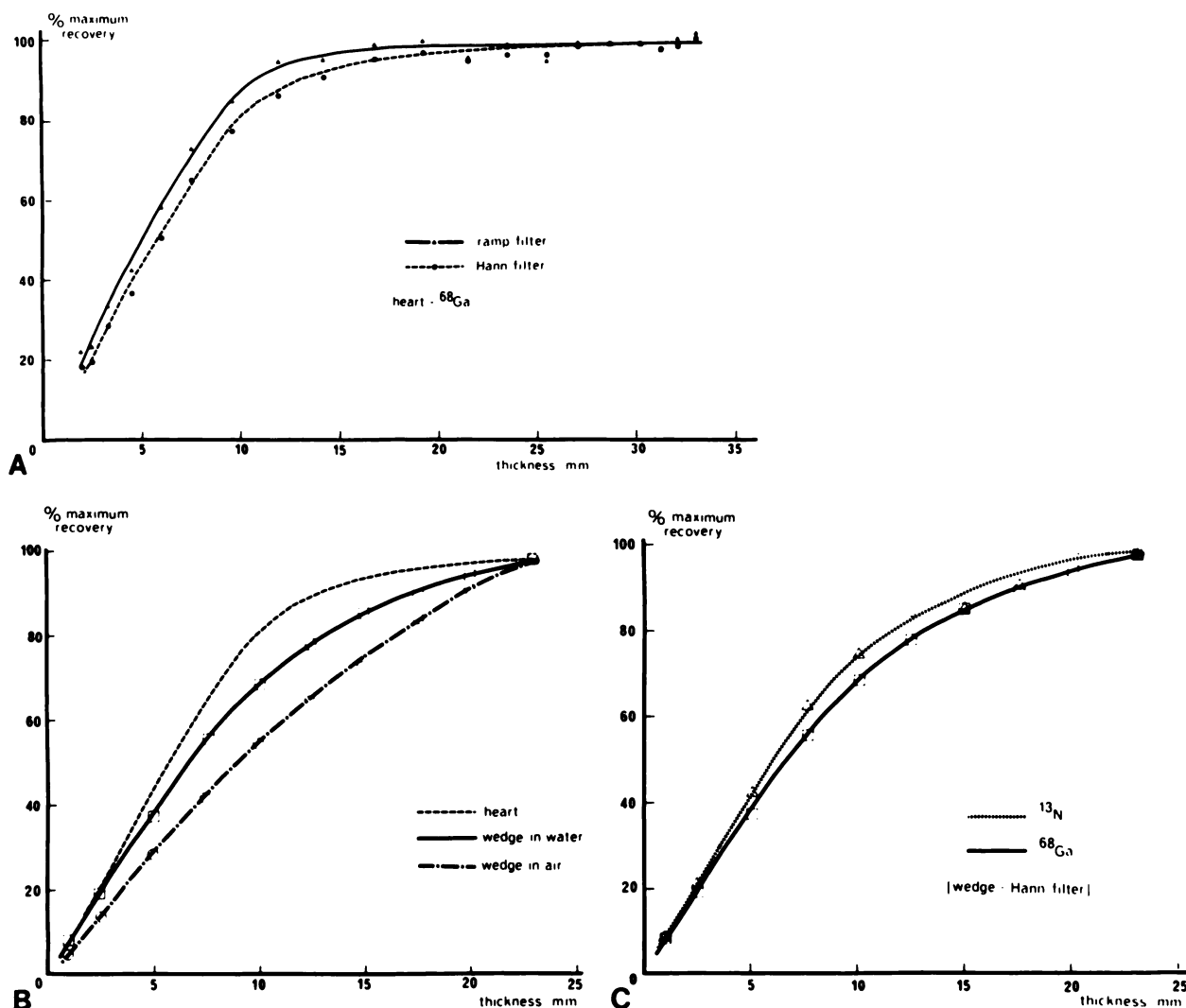


FIGURE 4
 A: Count recovery as a function of radial thickness of "myocardium" of heart phantom for two reconstruction filters. The curves were normalized to the maximum for the ramp filter. B: Comparison of count recovery for heart and wedge phantoms using the Hann reconstruction filter. The curve for the heart is the same as that in A. The wedge curves are both normalized to the heart curve at 23 mm. C: Comparison of count recovery for ^{13}N and ^{68}Ga in the wedge phantom (surrounded by water).

of determining and, if necessary, subtracting the proportion of measured true coincidences which inevitably arise from scattered radiation is important. Finally, a knowledge of uncertainties due to counting statistics is required.

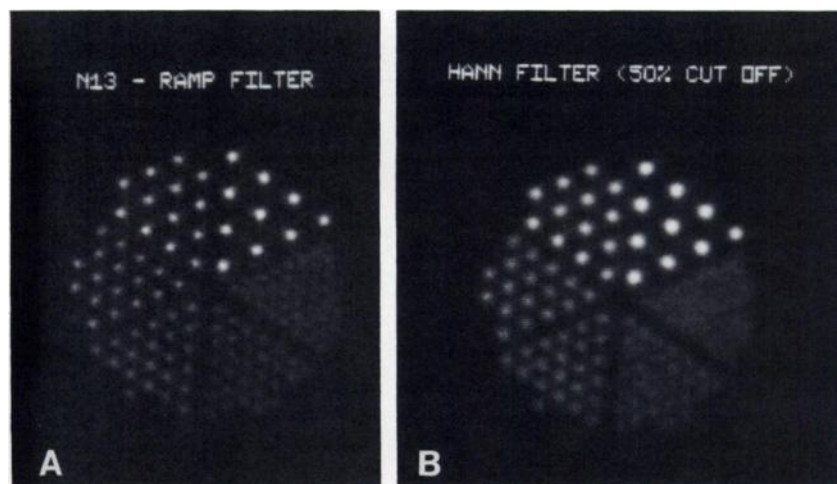
Even with improvements in design, assessment of such limitations is still relevant if the term absolute quantitation is to be used. The scanner in the present study represents a significant advance over previous generations (10). The use of small BGO detectors in a closely-packed ring yields improvement in spatial resolution and the ability to acquire dynamic data without detector motion.

In the assessment of count rate performance described above, the term deadtime loss (DTL) was applied for convenience of description but is not an entirely precise term. Losses due to deadtime are spe-

cifically those not recorded because the acquisition electronics is already busy. The losses which are relevant here also include those which are recorded but are not included in the true coincidences since they are in coincidence with one or more gamma rays in addition (i.e., multiples.) However, for the purposes of this discussion, the term DTL is kept. Empirical indices of DTL in other tomographs have been based on multiple rates (9) or random rates (11). For the scanner in this study, M does give an approximate index of DTL but appears to be slightly dependent on source geometry. Figure 2A shows that, for the same M, DTL is slightly higher for phantoms associated with more scatter (cylinder and tube source phantom) and hence a proportionally higher random rate (R). Specific deadtime loss in the acquisition electronics is basically dependent on the singles rates (S_1 and S_2) in opposing detectors. These

FIGURE 5

Images (direct plane) of multiple line source phantom reconstructed with measured attenuation correction and (A) ramp and (B) Hann filters. 750k true events were acquired in stationary mode.



are in turn related to R by the well-known expression:

$$R = S_1 S_2 \times 2\tau, \quad (2)$$

where 2τ is 24 nsec for this system. Therefore, a higher random rate means a higher singles rate with a consequently higher electronic deadtime. Measurement of the total loss of true events should thus take into account both multiple and random rates. Indeed, Figure 2B shows that the sum of M and R for the total system gives an empirical index of DTL that does not depend significantly on geometry.

The basic concern in obtaining accurate quantitation is that the measured image counts in a given region of interest (ROI) are proportional to the activity contained in that region (volume). A typical calibration procedure consists of relating ROI counts to the count rate in a sample taken from the object scanned and measured in a well counter. This allows the derivation of physiological parameters, such as blood flow from a tracer model, by comparing tissue (ROI) and blood (well counter) activity concentrations. The results of this study have demonstrated the dependence of image counts on the geometry of the scattering medium surrounding an active volume. This dependence is separate from the variation in recovery coefficients caused by object dimensions being less than about twice transaxial resolution (12).

In summary, this study has shown that the ECAT III has a spatial resolution of 6 to 8 mm (depending on counting statistics) under the conditions relevant to clinical studies in this laboratory (where stationary sampling mode is used). The uniformity of both transaxial and axial resolution over a FOV large enough for most clinical studies is very good. A simple empirical algorithm for the determination of the loss of true coincidence events from a knowledge of random and multiple rates has been defined. It is evident that the effect of

scatter is significant and should be carefully considered in clinical studies. A correction procedure for scatter remains to be implemented and tested, and the effect of correction on the estimation of recovery coefficients for varying activity distributions elucidated.

ACKNOWLEDGMENTS

The authors thank Dr. P. Camici and Dr. G. Licitra for their comments and discussion; Dr. P. Salvadori and Mr. L. Fusani for the production of radionuclides; Dr. A. Benassi and Messrs. G. Puccini, A. Riva; and S. Bonani for technical assistance.

REFERENCES

1. Hoffman EJ, Ricci AR, van der Stee LMAM, et al. ECAT III—basic design considerations. *IEEE Trans Nucl Sci* 1983; 30:729–733.
2. Hoffman EJ, Phelps ME, Huang SC, et al. Dynamic gated and high resolution imaging with the ECAT III. *IEEE Trans Nucl Sci* 1986; 33:452–455.
3. Jones WF, Casey ME, Byars LG, et al. A VME bus-based, real time sorter design for positron emission tomography. *IEEE Trans Nucl Sci* 1986; 33:601–604.
4. Dent HM, Jones WF, Casey ME. A real time digital coincidence processor for positron emission tomography. *IEEE Trans Nucl Sci* 1986; 33:556–559.
5. Burgiss SG, Byars LG, Jones WF, et al. High resolution and high speed positron emission data acquisition. *IEEE Trans Nucl Sci* 1986; 33:489–491.
6. Budinger TF, Gullberg GT, Huesman RH. Emission computed tomography. In: Herman GT, ed. *Topics of applied physics, Vol. 32—image reconstruction from projections*. New York: Springer-Verlag, 1979:147–246.
7. Adams R, Hine GJ, Zimmerman CD. Deadtime measurements in scintillation cameras under scatter conditions simulating quantitative nuclear cardiology. *J Nucl Med* 1978; 19:538–544.
8. Derenzo SE, Budinger TF, Cahoon JL, et al. High resolution computed tomography of positron emitters.

- IEEE Trans Nucl Sci* 1977; NS-24:544–558.
9. Hoffman EJ, Phelps ME, Huang SC. Performance evaluation of a positron tomograph designed for brain imaging. *J Nucl Med* 1983; 24:245–257.
 10. Williams CW, Crabtree MC, Burgiss SG. Design and performance characteristics of a positron emission computed axial tomograph—ECAT II. *IEEE Trans Nucl* 1979; NS-26:619–627.
 11. Yamamoto S, Amano M, Miura S, et al. Deadtime correction method using random coincidence for PET. *J Nucl Med* 1986; 27:1925–1928.
 12. Hoffman EJ, Huang SC, Phelps ME. Quantitation in positron emission computed tomography. 1. Effect of object size. *J Comput Assist Tomogr* 1981; 3:299–308.